Reproducible Ultrathin Ferroelectric Domain Switching for High-Performance Neuromorphic Computing

Jiankun Li, Chen Ge,* Jianyu Du, Can Wang, Guozhen Yang, and Kuijuan Jin*

Neuromorphic computing consisting of artificial synapses and neural network algorithms provides a promising approach for overcoming the inherent limitations of current computing architecture. Developments in electronic devices that can accurately mimic the synaptic plasticity of biological synapses, have promoted the research boom of neuromorphic computing. It is reported that robust ferroelectric tunnel junctions can be employed to design high-performance electronic synapses. These devices show an excellent memristor function with many reproducible states (≈200) through gradual ferroelectric domain switching. Both short- and long-term plasticity can be emulated by finely tuning the applied pulse parameters in the electronic synapse. The analog conductance switching exhibits high linearity and symmetry with small switching variations. A simulated artificial neural network with supervised learning built from these synaptic devices exhibited high classification accuracy (96.4%) for the Mixed National Institute of Standards and Technology (MNIST) handwritten recognition data set.

The rapid developments in intelligent tasks, such as artificial intelligence, big data analytics, autonomous vehicles, speech and image recognition, have put forward higher requirements for calculation speed and energy consumption.[1,2] The improvement of computer operation speed is limited by the data transfer rate between the central processing unit and the memory in the conventional von Neumann architecture. The human brain, which contains about 10^{11} neurons with 10^{15} interconnecting synapses, is particularly efficient at storing and processing information simultaneously (**Figure 1**a) with extremely

low energy (around 1–10 fJ per event).[3] The human brain has a special architecture that can perform massive parallel operating and solve complex problems. Therefore, simulating the operation of the human brain provides a route for confronting the bottleneck of von Neumann architecture.[4] Learning behavior in the human brain is achieved by reconfiguring the connection strength among synapses, which is called synaptic plasticity. Therefore, the construction of an artificial synaptic device that can emulate synaptic plasticity is a key step toward the realization of artificial neural networks.[5–10]

Two-terminal memristors with multiple intermediate conductance states are qualified synaptic devices that can resemble the brain synapse structure and perform a variety of synaptic plasticity tasks.[11] Various types of memristors, for example, conductive filament memories,[6,12–14] phase change memories (PCMs),[15,16] resistive switching memories based on ion migration,[17] and ferroelectric tunnel junctions (FTJs),[18] have been proposed for achieving high performance such as nonvolatility, a gradual resistance change, a threshold feature, a simple structure, and energy efficiency.[19] Among these devices, a promising candidate for mimicking artificial synaptic devices and performing neural network operations is FTJ,[18] which is an ultrathin ferroelectric film sandwiched by two electrodes whose resistance depends on the polarization direction (Figure 1b).[20–23] The pioneering work by Chanthbouala et al. demonstrated that the gradual switching of the ferroelectric domain and the resulting change of resistance states can ensure a memristor response in FTJs.[21] Subsequently, several works have explored the possibility of FTJs as artificial synapses.[18,24,25] Recently, Boyn et al. realized unsupervised learning using FTJ based simulations.[26]

In this work, we demonstrate an artificial synapse with ultralow femtojoule energy consumption based on Pt/BaTiO$_3$/Nb-doped SrTiO$_3$ FTJ devices. FTJ devices with metal/ferroelectric/semiconductor structures features with an extra depletion region on the semiconductor surface at the high resistance states (HRSs).[20] By analyzing the time-dependent transport and piezoresponse force microscopy measurements, the domain switching dynamics of the FTJ devices were investigated. Essential synaptic plasticity was mimicked in this FTJ device. The present device exhibits the coexistence of good short-term and long-term plasticity, and it is different from previous studies on long-term plasticity. Two different databases,

Dr. J. Li, Prof. C. Ge, J. Du, Prof. C. Wang, Prof. G. Yang, Prof. K. Jin
Beijing National Laboratory for Condensed Matter Physics
Institute of Physics
Chinese Academy of Sciences
Beijing 100190, China
E-mail: gechen@iphy.ac.cn; kjjin@iphy.ac.cn

Prof. C. Ge, Prof. C. Wang, Prof. K. Jin
University of Chinese Academy of Sciences
Beijing 100049, China

Prof. C. Ge
Key Laboratory of Polar Materials and Devices
Ministry of Education
Shanghai 200241, China

Prof. C. Wang, Prof. K. Jin
Songshan Lake Materials Laboratory
Dongguan, Guangdong 523808, China

The ORCID identification number(s) for the author(s) of this article can be found under https://doi.org/10.1002/adma.201905764.
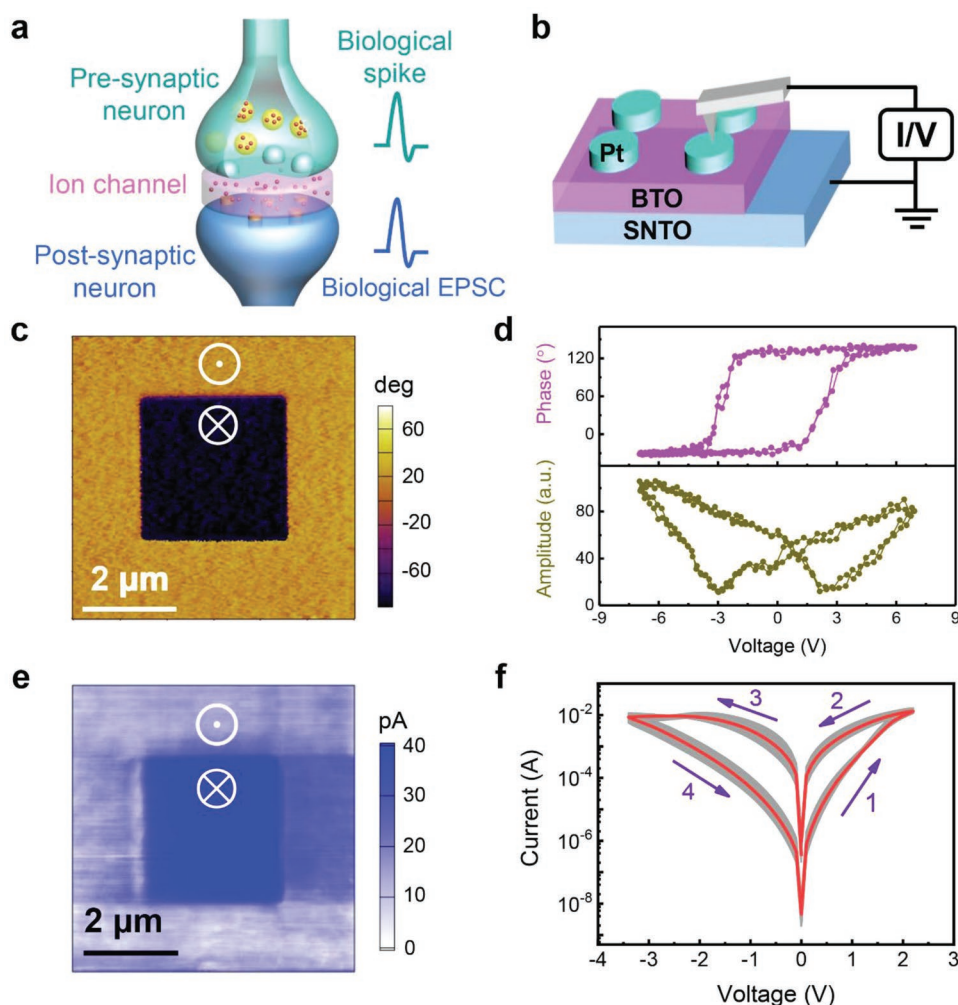
Figure 1. A schematic representation and electrical characterizations of the BTO based FTJ devices. a) A sketch of a biological synapse. b) A schematic illustration of a two-terminal Pt/BTO/SNTO FTJ device in which the Pt and SNTO electrodes mimic the pre- and postsynapse, respectively. c) A PFM out-of-plane phase contrast image of BTO/SNTO heterostructure. The two opposite phases were written by scanning the conductive-tip bias with ±6.5 V. d) The local phase (upper panel) and amplitude (lower panel) hysteresis loops of the BTO/SNTO heterostructure. e) A C-AFM image of the same area in (c). The read voltage was 0.5 V. f) Repeatable current–voltage loops for 300 cycles.

an 8 × 8 pixel image version (small image) of handwritten digits from the University of California at Irvine (UCI) image data set[27] and a 28 × 28 pixel image version (large image) of handwritten digits from the Mixed National Institute of Standards and Technology (MNIST) data set[28] were employed for image recognition. Supervised learning simulations in this work exhibited very high learning accuracies of 96.5% for the UCI image data set and 96.4% for the MNIST handwritten data set. Synaptic devices based on ultrathin ferroelectric domain switching open a novel approach for building efficient neuromorphic networks.

The ferroelectric tunnel junction, an ultrathin ferroelectric film sandwiched between two conductive electrodes, was fabricated to emulate biological synapses. High-quality $BaTiO_3$ (BTO) epitaxial films with a thickness of ≈2.8 nm were prepared on 0.7 wt% Nb-doped $SrTiO_3$ (SNTO) substrates through pulse laser deposition (PLD). A high deposited oxygen pressure of 20 Pa was used to avoid the effect of oxygen vacancy migration on our electronic synapses.[29] Using the standard

lithography technique, Pt circular electrodes with a thickness of 100 nm were patterned on the BTO films (see the Experimental Section).

The piezoresponse force microscopy (PFM) technique was employed to characterize the ferroelectricity of the BTO ultrathin film. Figure 1c shows the out-of-plane PFM image with writing voltages of ±6.5 V. The typical local PFM phase and amplitude hysteresis loops versus voltage are shown in Figure 1d. The clear domain boundary in Figure 1c and the 180° phase contrast in Figure 1d indicate that ferroelectric domains with opposite polarization directions can exist in the ultrathin BTO layer. In conjunction with the result of PFM, a conductive atomic force microscopy (C-AFM) measurement over the two antiparallel domains is also shown in Figure 1e. A DC bias of 0.5 V was applied to the polarization-patterned area to acquire the current mapping properties. The current of the domain exhibited an increase upon application of positive electric bias, which indicates a lower resistance state for the downward-polarized domain. After applying external bias, the

modification of the local conduction was more intuitive in the current–voltage (I–V) curves (Figure 1f). As shown in Figure 1f, typical I–V loops for 300 cycles with good reproducibility were achieved, indicating good fatigue property of the devices. In fact, after more than 1.1×10^4 cycles, the device still maintained the pristine ON/OFF ratio of a few hundred (Figure S1, Supporting Information), which implies good endurance. The retention characteristic is another important parameter for evaluating the performance of the device. In the retention test with a read voltage of 0.05 V, both HRS and low resistance state (LRS) could be stable for more than 10^4 s at room temperature and for more than 4000 s at 100 °C (Figure S2, Supporting Information).

We confirmed the dominant role of ferroelectric domain switching in the BTO-based FTJs grown under high oxygen pressures, by comparing to nonferroelectric SrTiO$_3$ (STO)-based devices.[29] **Figure 2**a exhibits the evolution of conductance-voltage (G–V) hysteresis loops as the pulse width varies while keeping the voltage range between −3.4 and +2.2 V. The conductance of LRS increases gradually as the pulse width increases, and eventually, a saturation value is reached when the pulse width is more than 10 ms. The conductance states of FTJ can be finely adjusted depending on the pulse amplitude and duration (Figure S3, Supporting Information). Here, the switching kinetics of the ferroelectric domains is crucial for modulating multilevel conductance states and realizing memristor function in FTJs. It has been widely accepted that the nucleation process of the ferroelectric domain and the propagation of domain walls in ferroelectric thin films can

be described well by the nucleation-limited-switching (NLS) model.[30] In the NLS model, several areas have inhomogeneous polarization switching and independent switching kinetics. The time-dependent change in the reverse area (S) can be written as follows[31]

$$S_{ON} = \int_{-\infty}^{+\infty} \left\{ 1 - \exp\left[-\left(\frac{t}{t_0} \right)^n \right] \right\} F(\log t_0) \, d(\log t_0) \tag{1}$$

where S_{ON} is the normalized down polarized area, n is the effective dimension, t_0 is the characteristic switching time for the domain growth, and $F(\log t_0)$ can be described as Lorentzian distribution

$$F(\log t_0) = \frac{A}{\pi} \left[\frac{w}{(\log t - \log t_0)^2 + w^2} \right] \tag{2}$$

where A is the normalization constant and w is the half-width of half-maximum.

In ultrathin ferroelectric films, the junction conductance G can be simplified as a parallel connection of small conductance with up polarization (G_{ON}) and large conductance with down polarization (G_{OFF}):

$$G = (1 - S_{ON}) \times G_{OFF} + S_{ON} \times G_{ON} \tag{3}$$

Hence, S_{ON} of the middle conductance states can be rewritten as

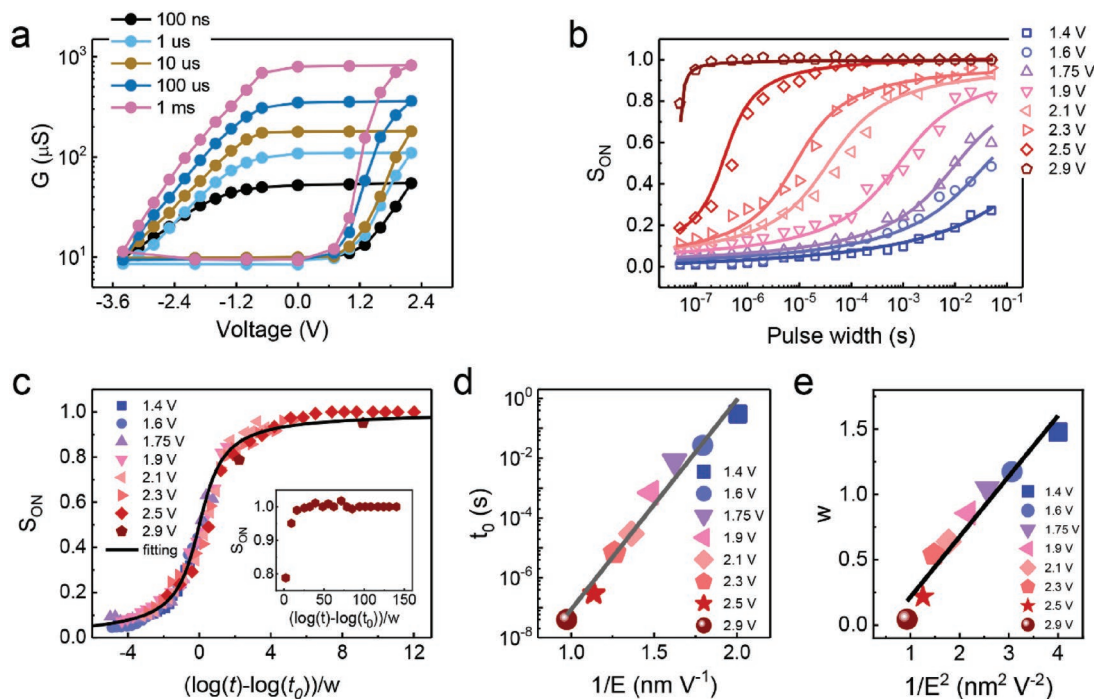$$S_{ON} = \frac{ratio - 1}{ratio_{max} - 1} \tag{4}$$

Figure 2. The domain switching kinetics of the FTJ device governed by nucleation-limited-switching model. a) Multiple G–V hysteresis loops as a function of pulse width. b) The normalized reversed areas as a function of pulse width under various pulse amplitudes. The lines are calculated from the NLS model. c) The rescaled normalized reversed areas as a function of fitting parameters for the NLS model. d) The evolution of the switching time as a function of the inverse of the positive switching field, which complies with Merz's Law. e) Switching field-dependent half-width of the half-maximum of the Lorentz distribution.

ADVANCED
SCIENCE NEWS
www.advancedsciencenews.com

ADVANCED
MATERIALS
www.advmat.de

where "ratio" is the ratio of the conductance of the middle conductance states to G_{OFF} and the $ratio_{max}$ is the ON/OFF ratio of the devices.

Figure S4 (Supporting Information) shows the conductance ratios under single pulses with different pulse amplitudes and widths. The device was pre-poled by negative pulses of −5 V and 1 μs before applying the write pulses. The ratio remained almost unchanged when the amplitude and width of the pre-spike were relatively small. Subsequently, the conductance ratio increased gradually and then reached a saturation value (≈500). According to Equation (4), the values of S_{ON} were extracted from Figure S4 (Supporting Information) and were plotted as data points in Figure 2b. The experimental S_{ON} could be reproduced well by Equation (1) with $n = 2$ (the lines in Figure 2b), indicating that the NLS model provided a good agreement with our results. If S_{ON} is rescaled by $(\log t - \log t_0)/w$, all curves overlap into a single arctangent curve (Figure 2c). The scaling behavior suggests that the Lorentzian fit accounts for the switching behavior, which means independent switching kinetics always dominate in our devices. Figure S5 (Supporting Information) presents the Lorentzian distribution functions of different bias, illustrating the main trends of t_0 and w with the

magnitude of the electric field. As the bias increases, t_0 and w show significant decreases. The evolution of $\log (t_0)$ versus $1/E$ (Figure 2d) and w versus $1/E^2$ (Figure 2e) demonstrate that $\log (t_0)$ and w were proportional to their abscissas. The exponential dependence of t_0 on $1/E$ (Figure 2d) is consistent with Merz's law ($t_0 \propto \exp(E_0/E)$, where E_0 is the activation field of about 7 V nm^{-1}).[32] The gradual switching process of polarization was also confirmed by the PFM phase and amplitude plots with varying pulse durations (Figure S6, Supporting Information). All these results confirm the gradual manipulation of the ferroelectric domain accompanied with multilevel conduction states in FTJs, which can be harnessed to construct artificial synapses.

Synaptic plasticity (short-term plasticity and long-term plasticity) is the basis for synapses to execute signal processing and neural computation. The synaptic weight can be updated temporarily (short-term plasticity, STP) or permanently (long-term plasticity, LTP) based on the ferroelectric polarization switching dynamics as a function of pulse amplitude and repetition. Typical STP behaviors based on the FTJ devices are emulated by applying low biases (**Figure 3**a). Excitatory postsynaptic currents (EPSCs) are triggered by the presynaptic spikes and decay gradually to the pristine current, reflecting the temporal
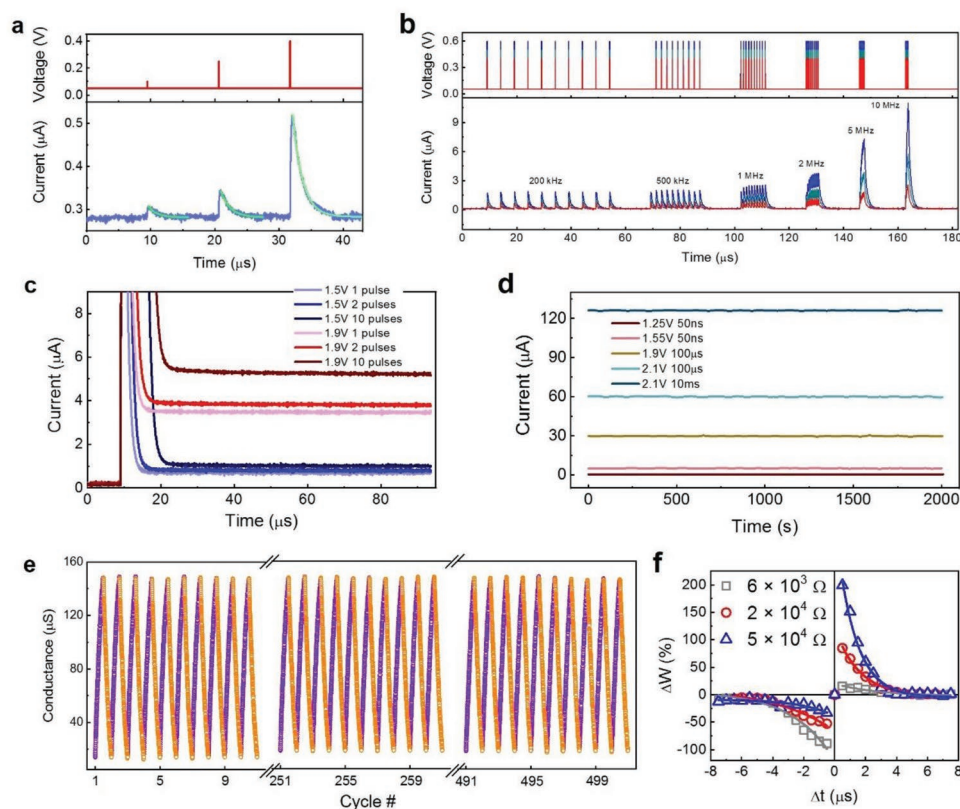

Figure 3. The pulse training, evolution of EPSC, and STDP characteristics of the Pt/BTO/SNTO device. a) The instantaneous current triggered by a presynaptic spike. The upper panel shows the shape of the applied voltage pulse, which consisted of a read voltage of 0.05 V and programming voltages of 0.1, 0.25, and 0.4 V with the duration of 50 ns. The green curves are the fitting lines. b) The EPSCs recorded in response to the stimulus train with six frequencies in the short-term potentiation mode. The pulse amplitudes were 0.4, 0.5, and 0.6 V, respectively. The pulse width was 50 ns. c) The device's relaxation performance showing the variation of current with different pulse numbers and amplitudes in the LTP mode. The pulse width was 50 ns and the pulse interval was 500 ns. d) The retention properties of the middle states for 2×10^3 s. e) Long-term potentiation and depression demonstrating 200 discrete states for 500 cycles. The potentiating and depressing pulses were +1.3 and −1.75 V in amplitude, respectively, and 50 ns in width. f) Weight-dependent STDP learning with an antisymmetric Hebbian learning rule. The synaptic weight (current) changes as a function of Δt. The solid lines show the fitting results according to Equation (5).

strengthening connection of two adjacent synapses. The calculated capacitance by fitting the relaxation currents (Figure 3a) is in good agreement with the measured value (Figure S7 and Note S1, Supporting Information). Thus, the STP behavior in our FTJs is ascribed to the charging and discharging process of the depletion region at HRS. In the STP mode, the response of the artificial synapse to the pulse stimulation signal is unaffected by the previous pulse when the pulse interval exceeds the time during which EPSC decays to the resting state (Figure S8, Supporting Information). The calculated energy consumption per spike (0.2–146 fJ) with a pulse width of 20 ns was several orders of magnitude lower than that (≈900 pJ) of artificial synapses based on conventional complementary metal-oxide semiconductor (CMOS) circuits, and can be compared with that (1–10 fJ) of human synapses (Figure S9, Supporting Information). If the interval between the stimulus pulses is shorter than the EPSC recovery time, then the synaptic response to the previous stimulus signal enhances the response to the following stimulus signal. Figure 3b shows the EPSC responses with varying presynaptic stimulus trains with different frequencies. The presynaptic stimulus train at each frequency consisted of 10 pulses with a pulse width of 50 ns and pulse amplitudes of 0.4, 0.5, and 0.6 V, respectively. The temporal increased currents exhibits a strong dependence on the pulse amplitude and frequency. We investigated the effects of the pulse duration and interval on the EPSC (Figure S10, Supporting Information). The increase of the pulse duration can enhance the EPSC, and the decrease of the pulse interval can also enhance the EPSC. Paired-pulse facilitation (PPF) is one of the most well-known physiological characteristics in recoding temporal information.[3,33] PPF is a form of STP phenomena, depicting the apparent enhancement of EPSC evoked by the second pulse. In FTJ devices, electric stimuli can be used to simulate the PPF phenomena. Figure S11 (Supporting Information) demonstrates the PPF characteristic of the FTJ device, and the initial state has little effect on the PPF property. If successive stimuli with pulse intervals that are comparable or shorter than the relaxation time of the EPSC are applied to the FTJ device, then the EPSCs of the following pulse are effectively potentiated (Figure S11, Supporting Information). This result shows the designed FTJ device had good short-term plasticity. Note S2 (Supporting Information) provides additional calculation details about PPF process. The device would show a paired-pulse depression (PPD) behavior, with a smaller pulse voltage, shorter pulse width, and longer pulse interval (Figure S12, Supporting Information).

The transition from STP to LTP in FTJs can be realized by applying presynaptic pulse amplitudes larger than the threshold voltage of the ferroelectric domain switching. Figure 3c illustrates the EPSCs obtained by applying stimuli with different pulse amplitudes and numbers. The pulse width and pulse interval were fixed to 50 and 500 ns, respectively. The training results show that the postsynaptic currents presented obvious potentiation and could not decay to the pristine value after modification by the presynaptic spikes, which suggests the existence of a long-term memory effect in the FTJ device. As the amplitude and number of the presynaptic spike increases, the current of the postsynapse increases significantly, corresponding to the enhancement of synaptic weight. More single pulses with different amplitudes and widths are applied to exhibit the

multilevel resistance states (Figure S13, Supporting Information). The intermediate conductance states showed good stability and remained unchanged for more than 2×10^3 s (Figure 3d). The transition from STP to LTP could occur with an increase in the pulse frequency (Figure S14, Supporting Information).

LTP usually consists of long-term potentiation and long-term depression, and it is the core design requirement for brain-like computing. Long-term potentiation is widely considered to be the main mechanism for learning and memory. Long-term potentiation effectively enhances the synaptic weight and maintains this enhancement for a long time. In contrast, long-term depression is an important mechanism with the opposite function to long-term potentiation. This means that the synaptic weight is modified from high to low and the connection between two neurons becomes weaker. Long-term depression contributes to forgetting memories and information storage. By alternately applying a series of 200 identical pulses (+1.3 and −1.75 V, 50 ns), long-term potentiation and depression with high-density nonvolatile states were obtained within a specific conductance range of 12–150 µS (Figure 3e). The long-term potentiation and depression processes for one cycle are shown in Figure S15 (Supporting Information). Figure S16 (Supporting Information) shows a typical current curve during the application of the pulses. A parameter ΔG is introduced to indicate the conductance change after two adjacent pulses. The obtained stepped conductance states in both the rising and falling processes showed stable values. In addition, the conductance state exhibits a linear relation with the ferroelectric domain evolution (Equation (3)), which allows the introduction of less additional "errors" for neural network calculation. Five hundred potentiation and depression cycles could be mimicked continuously by applying consecutive negative and positive spikes, reflecting reproducible switching. These results confirm good long-term plasticity in this FTJ device.

Spike-timing-dependent plasticity (STDP) is referred as being a form of Hebbian learning to illustrate the synaptic modification affected by the relative timing of fired spikes of connected neurons. It often plays a major role in information processing or brain network functions.[34,35] The synaptic weight increases and long-term potentiation occurs when a presynaptic spike is triggered momentarily (tens of nanoseconds) ahead of a postsynaptic spike ($\Delta t > 0$, where Δt is the relative time interval of the pre- and postsynaptic spikes). In contrast, when the order is reversed ($\Delta t < 0$), the synaptic weight decreases and long-term depression occurs. Meanwhile, the sign and magnitude of the change of synaptic weight precisely rely on Δt. As mentioned before, the top and bottom electrodes of the FTJ device can be regarded as the pre- and postsynaptic neurons, respectively. STDP forms with microsecond-scale times (four orders of magnitude faster than that in the human brain) were achieved in our FTJ device. Antisymmetric Hebbian learning STDP forms were implemented by following the typical series of spikes used in biological synapses and electronic synapses (Figure 3f). ΔW represents the nonvolatile modification of synaptic weight. The spike schemes of the pre- and postsynapse are demonstrated in Figure S17 (Supporting Information). The change of synaptic weight is a function of Δt: LTP occurs if $\Delta t > 0$ and LTD occurs if $\Delta t < 0$. The shorter the Δt is, the higher the obtained

ADVANCED
SCIENCE NEWS
www.advancedsciencenews.com

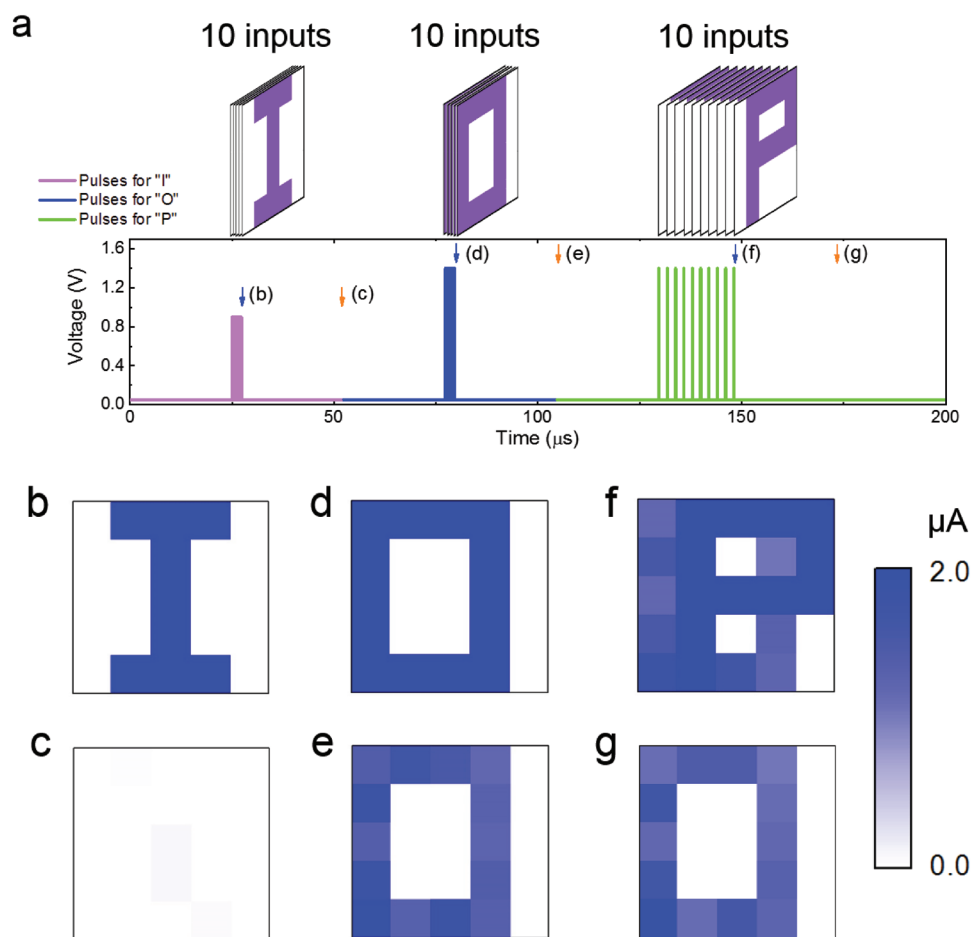**ADVANCED**
MATERIALS
www.advmat.de

Figure 4. The dynamic process of short-term potentiation and long-term potentiation in a 5 × 5 artificial synapse array. a) Images of the letters "I," "O," and "P," and the corresponding three kinds of pulse sequences, each of which consisted of ten consecutive stimulus pulses with duration of 50 ns, amplitudes of 0.9 and 1.3 V, pulse frequencies of 5 and 0.5 MHz, which were inputted into the synapse array for representing "I," "O," and "P." b,d,f) The images of "I," "O," and "P" just after the last pulse (expressed by the blue arrows in (a)). c,e,g) The images of "I," "O," and "P" at the 25 μs moment after the last pulse (expressed by the orange arrows in (a)). The letters "I" and "P" were memorized in the short-term potentiation mode and the letter "O" was memorized in the long-term potentiation mode.

ΔW is. Interestingly, in response to specific stimuli, the initial state was found to be an important parameter for the STDP characters (Figure 3f). As the resistance of the initial state decreases, a higher ΔW was obtained for the potentiation case and lower a ΔW is obtained for the depression case. The law of antisymmetric Hebbian learning STDP can be simply fitted through an exponential function, as follows

$$\Delta W = A \exp\left(\frac{-\Delta t}{\tau}\right) + W_0 \qquad (5)$$

where A is the scaling factor, τ is the time constant, and W_0 is a constant. The values of these parameters are summarized in Table S1 (Supporting Information). The fitting results are indicated by solid lines in Figure 3f. In addition to antisymmetric Hebbian learning, symmetric Hebbian learning STDP form was also simulated in the FTJ device. The synaptic spike scheme, experimental data, fitting formula, and fitting results are provided in Figure S18 (Supporting Information).

To prove the STP and LTP properties, the memorization of three letters with a 5 × 5 synapse array was initiated. The synapse array was operated on 25 individual FTJ devices. The electrical train memorized three letters in the synapse array: 1) a letter "I" via the STP mode was stored using 10 stimuli with a low amplitude of 0.9 V and a high frequency of 5 MHz; 2) a letter "O" via the LTP mode was stored using 10 stimuli with a high amplitude of 1.3 V and a high frequency of 5 MHz; 3) a letter "P" via the STP mode was stored using 10 stimuli with a high amplitude of 1.3 V and a low frequency of 0.5 MHz (**Figure 4**a). All the synapses were initialized to a high resistance state before electrical stimuli. The blue and orange arrows in Figure 4a indicate the event of the last pulse and the event 25 μs after the last pulse, respectively. Figure S19 (Supporting Information) shows a typical EPSC curve corresponding to the stimuli trains. After training with the letter "I," temporarily enhanced currents were rapidly attenuated to the initial state (Figure 4b,c). After training with the letter "O," long-term memory occurred and the EPSC becomes larger (Figure 4d,e). After training with the letter "P," short-term memory occurred. The excitatory pixels of the letter "O" are maintained after the pulses of "P" (Figure 4f,g). In summary, only the letter "O" was

memorized after the electrical training process because of its long-term memory nature. Separate processes for each letter "I," "O," and "P" are illustrated in Figures S20–S22 (Supporting Information), respectively. This experimental result clearly showed both good STP and LTP properties in one FTJ device.

Simulations of supervised learning using experimental long-term potentiation and depression were carried out based on a back propagation algorithm (**Figure 5**a). Here, the 8×8 pixel image version (small image) of handwritten digits from the UCI image data set,[27] and the 28×28 pixel image version (large image) of handwritten digits from the MNIST handwritten data set[28] were utilized for learning. A crossbar with N input rows (green horizontal lines) and M output columns (blue vertical lines) was employed to carry out the weight updates for matrix operations (Figure 5b). In the back propagation algorithm, the crossbar was used to perform the vector-matrix multiplication and outer product update operations as part of a "neural core." In order to properly simulate the device nonideality, the data in the long-term potentiation and depression processes were analyzed in detail. The cycle-to-cycle variation is characterized in Figure 5c, in which the conductance at each resistance state showed minor changes over 500 switching cycles.

The minor conductance variation facilitates a reduction of the writing noise during the training process.[36,37] In addition to the conductance variation between cycles, the linearity of the weight update in the long-term potentiation and depression processes can also significantly affect the accuracy of the
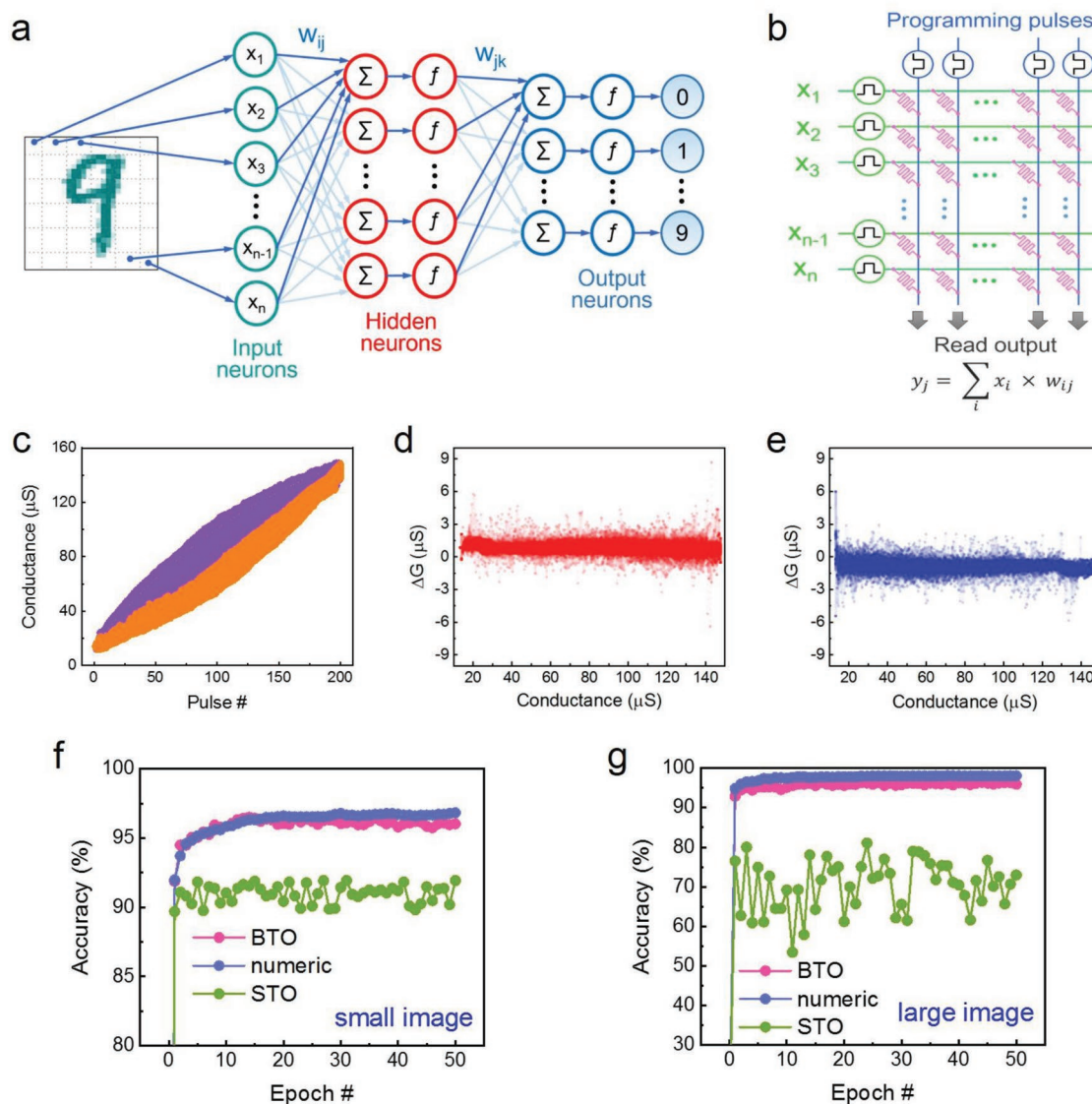

Figure 5. The simulation of back propagation in the FTJ device. a) A schematic diagram of a three layer neural network. b) A schematic diagram of a neural core with a crossbar structure to perform the analog matrix operations. The grayscale of each pixel is represented by the value of input voltage and the output value is represented by the value of output current. The synaptic weight is indicated by the conductance of each resistive memory. c) The overlapping plot of the long-time potentiation and depression processes over 500 cycles. The statistical ΔG versus conductance plots for d) potentiation and e) depression. The training accuracy of BTO and STO based devices for f) a small image and g) a large image.

training process. Here, the linearity of the weight update can be defined quantitatively as[38]

$$L = \frac{\max \left| G_P(n) - G_D(201-n) \right|}{G_P(200) - G_P(1)} \text{ for } n = 1 \text{ to } 200 \qquad (6)$$

where $G_P(n)$ and $G_D(n)$ are the conductance values after the nth potentiation pulse and nth depression pulse, respectively. For an ideal linear update case, linearity should be zero. The switching linearity of our FTJ-based device is the best one among two-terminal electronic synapses, to the best of our knowledge (Table S2, Supporting Information). It is only poorer than several three-terminal electrolyte-gated synaptic transistors, which decouple the write/read processes by using an additional gate terminal. The conductance deviation between experimental values of long-term potentiation and depression processes is plotted in Figure 5d,e, respectively. The neural network training[39] based on this BTO FTJ device achieved a high recognition accuracy (Figure 5f,g). The results of the training were comparable to the ideal accuracy, which represents the neural network algorithm limit. For recognizing a small image, an accuracy as high as 96.5% was achieved. The accuracy for recognizing large image approached 96.4%, which is a little lower than the numeric accuracy of 98%. However, the classification accuracies are only about 92% and 70% for small and large images in STO-based synapses with resistive switching, respectively. Table S2 (Supporting Information) shows the state-of-the-art device performance of the artificial synapses. Our well-designed synaptic device showed good performance in not only ferroelectric based devices but also other conductive filaments, ion migration, and phase change based memristive devices.

In conclusion, we presented high-performance electronic synapses with ultralow femtojoule energy consumption, fast operation speed, and high "write" linearity using FTJs. By finely tuning the applied pulse parameters, the device can emulate both short- and long-term plasticity. These types of artificial synapses emulate various biological synaptic plasticity by harnessing robust ferroelectric domain switching dynamics accompanied by the manipulation of the conductance states. One simple application by using both LTP and STP is emulating associative learning with the famous classical conditioning Pavlov's dog experiments.[40] More importantly, we think that coexistence of LTP and STP in the same device could enable designing efficient brain-like architectures. A simulated artificial neural network with supervised learning consisting of these synaptic devices exhibited very high learning accuracies of 96.5% for the UCI image data set and 96.4% for the MNIST handwritten data set. These results demonstrate the device's potential through ferroelectric domain switching for applications in energy-efficient neuromorphic computing.

Experimental Section

Device Preparation: BTO and STO epitaxial films were grown by PLD on (001)-oriented SNTO single-crystalline substrates using a XeCl excimer laser with a wavelength of 308 nm and a repetition rate of 2 Hz. The BTO films were deposited at 750 °C and cooled down to room temperature at 20 °C min⁻¹ in a flowing oxygen atmosphere of 20 Pa. The STO films were deposited at 750 °C and cooled down to room temperature at 20 °C min⁻¹ in a flowing oxygen atmosphere of 1 Pa. The deposition rate of BTO and STO films was calibrated by X-ray Reflection (XRR). Top platinum electrodes with a radius of 10 μm were fabricated on the films using ultraviolet lithography and e-beam evaporation.

Characterization: The surface morphology, PFM imaging, local ferroelectric properties, and current mapping of BTO/SNTO heterostructure were performed using a commercial scanning probe microscope (Asylum Research MFP3D). Pt/Ti-coated silicon cantilevers were used for the surface morphology and PFM imaging. Conductive-diamond-coated silicon cantilevers were adopted in the C-AFM measurements. Local hysteretic behaviors of the PFM phase and amplitude signals were collected in DART (dual A.C. resonance tracking) mode and the signals were recorded while the voltage was off. High quality of BTO epitaxial films was confirmed by scanning transmission electron microscopy measurements.[29]

Electrical Measurements: Electrical measurements were performed in vacuum by a Keithley 4200 semiconductor analyzer with 4225-PMU Ultra-Fast IV Modules. The shortest pulse that the ultrafast module could generate was 20 ns. The FTJ sample was placed in a LakeShore TTPX cryogenic probe station with 3 μm W probes. The test pulses were applied to the Pt top electrodes and the SNTO substrates were grounded, where positive bias means currents flow from the metal electrodes to the SNTO substrates.

Neural Network Simulations: The performance of a neural network was simulated on the basis of the platform CrossSim.[36] The simulator was based on backpropagation algorithm using experimentally measured conductance levels, linearity, and noise.[39,41] As shown in Figure 5a, the simulated neural network consisted of three layers including the input layer, hidden layer, and output layer. It was implemented by two crossbars. The number of input points was dependent on the number of image pixels, and the number of output points was dependent on the number of images to be identified. For small images (8 × 8 pixels), the network size of 64 (input layer) × 36 (hidden layer) × 10 (output layer) was used. Hence, the first crossbar structure comprised 64 input lines and 36 output columns. The data for each pixel were input at the same time. The number of inputs of the second crossbar was the same as the number of outputs of the first crossbar. The second crossbar structure comprised 36 input lines and 10 output columns. After training with 3823 images, the system was used to recognize a separate 1979-image testing set. For large images (28 × 28 pixels), the network size was 784 × 300 × 10. A 60 000-image training set and a 10 000-image testing set were used.

Supporting Information

Supporting Information is available from the Wiley Online Library or from the author.

Acknowledgements

Conflict of Interest

The authors declare no conflict of interest.

[1] L. Yann, B. Yoshua, H. Geoffrey, *Nature* **2015**, *521*, 436.
[2] M. A. Zidan, J. P. Strachan, W. D. Lu, *Nat. Electron.* **2018**, *1*, 22.
[3] J. T. Yang, C. Ge, J. Y. Du, H. Y. Huang, M. He, C. Wang, H. B. Lu, G. Z. Yang, K. J. Jin, *Adv. Mater.* **2018**, *30*, 1801548.
[4] P. Yao, H. Wu, B. Gao, S. B. Eryilmaz, X. Huang, W. Zhang, Q. Zhang, N. Deng, L. Shi, H.-S. P. Wong, H. Qian, *Nat. Commun.* **2017**, *8*, 15199.
[5] H. Mulaosmanovic, E. Chicca, M. Bertele, T. Mikolajick, S. Slesazeck, *Nanoscale* **2018**, *10*, 21755.
[6] Y. Shi, X. Liang, B. Yuan, V. Chen, H. Li, F. Hui, Z. Yu, F. Yuan, E. Pop, H.-S. P. Wong, M. Lanza, *Nat. Electron.* **2018**, *1*, 458.
[7] S. Ambrogio, P. Narayanan, H. Tsai, R. M. Shelbym I. Boybat, C. Nolfo, S. Sidler, M. Giordano, M. Bodini, N. C. P. Farinha, B. Killeen, C. Cheng, Y. Jaoudi, G. W. Burr, *Nature* **2018**, *558*, 60.
[8] W. Xu, S.-Y. Min, H. Hwang, T.-W. Lee, *Sci. Adv.* **2016**, *2*, e1501326.
[9] X. Zhu, D. Li, X. Liang, W. D. Lu, *Nat. Mater.* **2019**, *18*, 141.
[10] H. Mulaosmanovic, T. Mikolajick, S. Slesazeck, *IEEE Electron Device Lett.* **2018**, *39*, 135.
[11] M. Prezioso, F. M. Bayat, B. D. Hoskins, G. C. Adam, K. K. Likharev, D. B. Strukov, *Nature* **2015**, *521*, 61.
[12] B. C. Jang, S. Kim, S. Y. Yang, J. Park, J. Cha, J. Oh, J. Choi, S. G. Im, V. P. Dravid, S. Choi, *Nano Lett.* **2019**, *19*, 839.
[13] S. Choi, S. H. Tan, Z. Li, Y. Kim, C. Choi, P. Chen, H. Yeon, S. Yu, J. Kim, *Nat. Mater.* **2018**, *17*, 335.
[14] Z. Wang, S. Joshi, S. Savel'ev, W. Song, R. Midya, Y. Li, M. Rao, P. Yan, S. Asapu, Y. Zhuo, H. Jiang, P. Lin, C. Li, J. H. Yoon, N. K. Upadhyay, J. Zhang, M. Hu, J. P. Strachan, M. Barnell, Q. Wu, H. Wu, R. S. Williams, Q. Xia, J. J. Yang, *Nat. Electron.* **2018**, *1*, 137.
[15] T. Tuma, A. Pantazi, M. Le Gallo, A. Sebastian, E. Eleftheriou, *Nat. Nanotechnol.* **2016**, *11*, 693.
[16] D. Kuzum, R. G. Jeyasingh, B. Lee, H. S. Wong, *Nano Lett.* **2012**, *12*, 2179.
[17] E. E. Josberger, Y. Deng, W. Sun, R. Kautz, M. Rolandi, *Adv. Mater.* **2014**, *26*, 4986.
[18] S. Majumdar, H. Tan, Q. H. Qin, S. van Dijken, *Adv. Electron. Mater.* **2019**, *5*, 1800795.
[19] M. L. Schneider, C. A. Donnelly, S. E. Russek, B. Baek, M. R. Pufall, P. F. Hopkins, P. D. Dresselhaus, S. P. Benz, W. H. Rippard, *Sci. Adv.* **2018**, *4*, e1701329.
[20] Z. Wen, C. Li, D. Wu, A. Li, N. Ming, *Nat. Mater.* **2013**, *12*, 617.
[21] A. Chanthbouala, A. V. Garcia, R. O. Cherifi, K. Bouzehouane, S. Fusil, X. Moya, S. Xavier, H. Yamada, C. Deranlot, N. D. Mathur, M. Bibes, A. Barthélémy, J. Grollier, *Nat. Mater.* **2012**, *11*, 860.
[22] Z. Wen, D. Wu, A. Li, *Appl. Phys. Lett.* **2014**, *105*, 052910.
[23] R. Guo, Y. Zhou, L. Wu, Z. Wang, Z. Lim, X. Yan, W. Lin, H. Wang, H. Y. Yoong, S. Chen, Ariando, T. Venkatesan, J. Wang, G. M. Chow, A. Gruverman, X. Miao, Y. Zhu, J. Chen, *ACS Appl. Mater. Interfaces* **2018**, *10*, 12862.
[24] S. Majumdar, B. Chen, Q. H. Qin, H. S. Majumdar, S. van Dijken, *Adv. Funct. Mater.* **2018**, *28*, 1703273.
[25] Z. Wang, B. Crafton, J. Gomez, R. Xu, A. Luo, Z. Krivokapic, L. Martin, S. Datta, A. Raychowdhury, A. I. Khan, in *2018 IEEE International Electron Devices Meeting (IEDM)*, IEEE, Piscataway, NJ **2018**.
[26] S. Boyn, J. Grollier, G. Lecerf, B. Xn, N. Locatelli, S. Fusil, S. Girod, C. Carrétéro, K. Garcia, S. Xavier, J. Tomas, L. Bellaiche, M. Bibes, A. Barthélémy, S. Saïghi, V. Garcia, *Nat. Commun.* **2017**, *8*, 14736.
[27] K. Bache, M. Lichman, *University of California at Irvine*, School of Information and Computer Science, Irvine, CA, USA **2016**.
[28] L. Yang, C. Cortes, C. J. Burges, *National Institute of Standards and Technology*, Gaithersburg, MD, USA **2016**.
[29] J. Li, N. Li, C. Ge, H. Huang, Y. Sun, P. Gao, M. He, C. Wang, G. Yang, K. Jin, *iScience* **2019**, *16*, 368.
[30] A. K. Tagantsev, I. Stolichnov, N. Setter, J. S. Cross, M. Tsukada, *Phys. Rev. B* **2002**, *66*, 214109.
[31] J. Y. Jo, H. S. Han, J.-G. Yoon, T. K. Song, S.-H. Kim, T. W. Noh, *Phys. Rev. Lett.* **2007**, *99*, 267602.
[32] W. J. Merz, *Phys. Rev.* **1954**, *95*, 690.
[33] J.-X. Bao, E. R. Kandel, R. D. Hawkins, *Science* **1997**, *275*, 969.
[34] J. M. Young, W. J. Waleszczyk, C. Wang, M. B. Calford, B. Dreher, K Obermayer, *Nat. Neurosci.* **2007**, *10*, 887.
[35] Z. Wang, S. Joshi, S. E. Savel'ev, H. Jiang, R. Midya, P. Lin, M. Hu, N. Ge, J. P. Strachan, Z. Li, Q. Wu, M. Barnell, G.-L. Li, H. L. Xin, R. S. Williams, Q. Xia, J. J. Yang, *Nat. Mater.* **2017**, *16*, 101.
[36] S. Agarwal, S. J. Plimpton, D. R. Hughart, A. H. Hsia, I. Richter, J. A. Cox, C. D. James, M. J. Marinella, *International Joint Conference on Neural Networks (IJCNN)*, IEEE, Vancouver, BC, Canada **2016**.
[37] H. Y. Yoong, H. Wu, J. Zhao, H. Wang, R. Guo, J. Xiao, B. Zhang, P. Yang, S. J. Pennycook, N. Deng, X. Yan, J. Chen, *Adv. Funct. Mater.* **2018**, *28*, 1806037.
[38] I.-T. Wang, C.-C. Chang, L-W. Chiu, T. Chou, T-H. Hou, *Nanotechnology* **2016**, *27*, 365204.
[39] Y. van de Burgt, E. Lubberman, E. J. Fuller, S. T. Keene, G. C. Faria, S. Agarwal, M. J. Marinella, A. A. Talin, A. Salleo, *Nat. Mater.* **2017**, *16*, 414.
[40] R. A. John, F. Liu, N. A. Chien, M. R. Kulkarni, C. Zhu, Q. Fu, A. Basu, Z. Liu, N. Mathews, *Adv. Mater.* **2018**, *30*, 1800220.
[41] E. J. Fuller, F. E. Gabaly, F. Léonard, S. Agarwal, S. J. Plimpton, R. B. Jacobs-Gedrim, C. D. James, M. J. Marinella, A. A. Talin, *Adv. Mater.* **2017**, *29*, 1604310.